PHYSICAL REVIEW APPLIED **15,** 034044 (2021)

Featured in Physics

Nongalvanic Calibration and Operation of a Quantum Dot Thermometer

J.M.A. Chawner,[1,*] S. Barraud,[2] M.F. Gonzalez-Zalba,[3,†] S. Holt,[1] E.A. Laird,[1] Yu. A. Pashkin,[1]
and J.R. Prance[1]

[1] *Department of Physics, Lancaster University, Lancaster LA1 4YB, United Kingdom*
[2] *CEA/LETI-MINATEC, CEA-Grenoble, Grenoble 38000, France*
[3] *Hitachi Cambridge Laboratory, J. J. Thomson Avenue, Cambridge CB3 0HE, United Kingdom*

(Received 11 August 2020; revised 12 November 2020; accepted 26 January 2021; published 16 March 2021)

A cryogenic quantum dot thermometer is calibrated and operated using only a single nongalvanic gate connection. The thermometer is probed with radio-frequency reflectometry and calibrated by fitting a physical model to the phase of the reflected radio-frequency signal taken at temperatures across a small range. Thermometry of the source and drain reservoirs of the dot is then performed by fitting the calibrated physical model to new phase data. The thermometer can operate at the transition between thermally broadened and lifetime-broadened regimes and outside the temperatures used in calibration. Electron thermometry is performed at temperatures between 3.0 K and 1.0 K, in both a 1-K cryostat and a dilution refrigerator. In principle, the experimental setup enables fast electron-temperature readout with a sensitivity of $4.0 \pm 0.3\ \mathrm{mK}/\sqrt{\mathrm{Hz}}$, at kelvin temperatures. The nongalvanic calibration process gives a readout of physical parameters, such as the quantum dot lever arm. The demodulator used for reflectometry readout is readily available at relatively low cost.

DOI: 10.1103/PhysRevApplied.15.034044

I. INTRODUCTION

The electron temperature is a fundamental parameter that can limit the performance of low-temperature experiments and applications. Electron thermometry is an essential tool in understating the behavior of low-temperature circuitry [1], for example, the processors used in quantum computers or devices used to study exotic electronic phases and materials. Accurate and fast electron-temperature readout is also a valuable tool for thermodynamic experiments. Increasingly sensitive quantum circuits require delicate and noninvasive electronic thermometry. Quantum dot (QD) and single-electron transistor (SET) conduction thermometry are well established as powerful approaches to the monitoring of electron temperatures [1–11]. However, these thermometers require the measurement of current through the QD, which can complicate or interfere with other electronic measurements in the experiment. Furthermore, the extra galvanic connections for dot thermometry can be a source of additional noise and parasitic heating. Local charge sensing can be used to probe the occupation of a QD without having to pass a direct current through it [5,12–15]. This approach still requires galvanic connections to read the charge sensor. Similarly, radio-frequency (rf) reflectometry techniques have recently allowed QD thermometry to be performed without measuring the current through the QD, which is effective outside the lifetime-broadened regime [16,17]. However, for both charge sensing and reflectometry, connections to the source and drain of the dot are still needed to measure the dot lever arm for calibration.

Here, we demonstrate how a completely nongalvanic QD thermometer can be calibrated and used with a single capacitive gate connection, including a calibration of the lever arm with no dc source-drain bias. The QD thermometer has the flexibility to be used on any conducting reservoir and operates in an intermediate regime where the maximum temperature is much lower than the QD charging energy $k_B T \ll E_c$ and the minimum temperature is similar to the tunnel coupling $k_B T \sim \hbar\Gamma$.

II. EXPERIMENTAL DETAILS

The QD device used in our experiment is a silicon-on-insulator trigate accumulation-mode field-effect transistor (FET) with a channel length, width, and height of 80 nm, 30 nm, and 10 nm, respectively, shown in Figs. 1(a) and 1(b).For more details of the device, see Ref. [18]. At cryogenic temperatures, when a positive subthreshold dc voltage V_{tg} is applied to the top gate, a localization potential appears in the Si channel underneath the gate. This allows bound electron states to accumulate and creates a

---

[*] j.chawner@lancaster.ac.uk

[†] Present address: Quantum Motion Technologies, Windsor House, Cornwall Road, Harrogate HG1 2PW, United Kingdom.

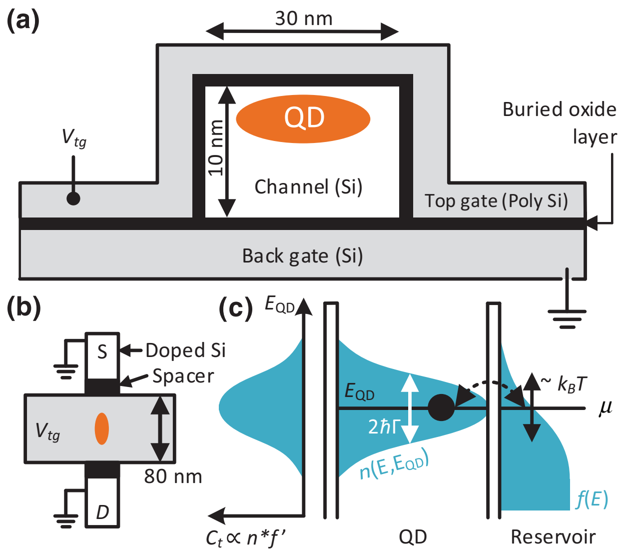

FIG. 1. Details of the silicon field-effect transistor QD. (a) A cross-section schematic of the device. The transistor consists of an undoped one-dimensional (1D) Si channel, 10 nm high by 30 nm wide, with n-doped Si source-drain connections. A polycrystalline silicon top gate, 80 nm wide, bridges over the channel, separated by a layer of SiO_2. A grounded Si back gate is located beneath the channel, separated from the channel by 145-nm-thick buried SiO_2. (b) The top view of the device. The source (S) and drain (D) channel connection points are n doped and behave as a single grounded reservoir during thermometry operation. Two spacers are used to prevent doping of the Si channel under the top gate. (c) The energy diagram of the system. The reservoir has an occupation of electron states given by the Fermi-Dirac distribution f. The QD energy level E_{QD} is broadened from tunnel coupling to the reservoir, with a density of states n described by Eq. (1). The tunneling capacitance C_t as a function of E_{QD} has a shape proportional to $f' * n$.

single QD. Corner dots [19,20] do not appear in the structure due to the narrow width of the channel. The FET top gate also acts as a plunger gate for the QD via capacitance C_{tg}, allowing tuning of the next available energy level in the QD, which is labeled E_{QD}, by adjusting V_{tg}. The source and drain electrodes are both grounded and act as a single reservoir of electrons with a Fermi level μ [Fig. 1(c)]. Throughout the experiment, the back gate is grounded.

The QD energy level E_{QD} is broadened by tunnel coupling to the reservoir [21,22]. This is described with a broadened density of states in the form of a normalized Lorentzian, given by

$$n(E_{QD}, E) = \frac{1}{\pi}\frac{\hbar\Gamma}{(E_{QD} - E)^2 + (\hbar\Gamma)^2}, \tag{1}$$

where $\hbar$ is the reduced Planck's constant [21]. The tunnel rate Γ between the QD and the reservoir is given by $\Gamma = \Gamma_s\Gamma_d/(\Gamma_s + \Gamma_d)$, where $\Gamma_{s(d)}$ is the tunnel rate through the source(drain) barrier. The probability P_{QD} of an excess electron occupying the QD is given by the integral of the product of $n(E_{QD}, E)$ and the Fermi-Dirac distribution of electrons in the reservoir $f(E)$ [21]:

$$P_{QD}(E_{QD}) = \int_{-\infty}^{\infty} f(E) n(E_{QD}, E) dE. \tag{2}$$

This is the convolution of the two functions, so P_{QD} becomes

$$P_{QD}(E_{QD}) = (f * n). \tag{3}$$

Due to the spin degeneracy of the extra electron in the QD, $P_{QD} = 1/2$ occurs when $E_{QD} = \mu \pm k_B T \ln 2$ [17,23]. The QD has both a constant geometric capacitance and a variable "tunneling" capacitance C_t, given by [17,24–28]:

$$C_t(V_{tg}) = e\alpha \frac{\partial P_{QD}}{\partial V_{tg}}, \tag{4}$$

where $\alpha = C_{tg}/C_\Sigma$ is the top-gate lever arm, C_Σ is the total QD capacitance, $\partial V_{tg} = -\partial E_{QD}/e\alpha$, and e is the elementary charge. Insertion of Eq. (3) into this definition gives us the tunneling capacitance of the QD-reservoir system:

$$C_t(V_{tg}) = e\alpha(f * n)' = e\alpha(f' * n). \tag{5}$$

The derivative of f with respect to V_{tg}, denoted f', is

$$f'(V_{tg}) = \frac{1}{4k_B T_e}\cosh^{-2}\left(\frac{-\alpha e(V_{tg} - V_0)}{2k_B T_e}\right), \tag{6}$$

where T_e is the electron temperature of the reservoirs, V_0 is the value of V_{tg} when $P_{QD} = 1/2$, and k_B is the Boltzmann constant. The T_e dependence of C_t via Eq. (6) is the basis for the nongalvanic QD thermometer.

The capacitance C_t is measured by rf reflectometry using the setup shown in Fig. 2(a). A resonant circuit is connected to the QD top gate and consists of a Nb-Ti-N-on-quartz spiral inductor $L = 96$ nH and a coupling capacitor $C_c = 0.18$ pF. The inductor is placed parallel to the measured capacitance to help improve the loaded Q factor, which helps achieve a larger signal for a given change in capacitance [29]. The modeling of the circuit using the measured rf reflection $|R|$ and phase ϕ [shown in Fig. 2(b)] gives a resonance frequency of $f_0 = 593.4$ MHz with a Q factor of 63, a parasitic capacitance of $C_p = 0.57$ pF, and a parasitic resistance of $R_p = 43.2$ kΩ. A modeled circuit loss to ground is represented by resistance R_p, which affects the resonance Q factor [29]. The parasitic capacitance C_p includes the geometric gate capacitance C_{tg}. The demodulation of $|R|$ and ϕ is performed using an "ADL5387" active-quadrature demodulator chip. To allow a dc bias V_{tg} to be applied to the top gate, a 100-pF capacitor is placed after the inductor to avoid dc shorting

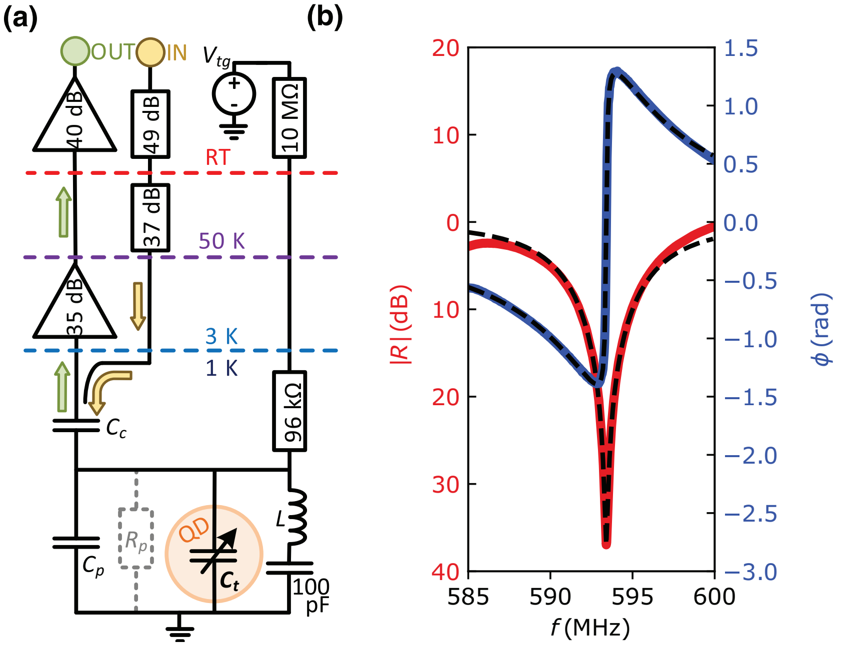

FIG. 2. Details of the rf circuitry. (a) A schematic of the circuit layout. The resonant circuit is comprised of the Nb-Ti-N-on-quartz spiral inductor L, the parasitic capacitance C_p, the coupling capacitance C_c, and the variable QD tunneling capacitance C_t, which is the physical parameter monitored for thermometry. C_p includes the geometric gate capacitance C_{tg} for modeling purposes. R_p is a modeled parasitic loss resistance to ground, which impacts the resonant circuit Q factor. The inductor line has a 100-pF capacitor to provide a dc break between the top gate and ground. The 96-kΩ resistor limits the top-gate rf signal loss to the dc line. V_{tg} is the controllable dc top-gate voltage. IN and OUT represent the rf reflectometry input and output signal, respectively. (b) The loaded measurement circuit resonance when coupled to the top gate, with the reflected-signal magnitude $|R|$ and phase ϕ shown in red and blue, respectively. The black dashed lines show the fitted circuit model, which measures a Q factor of 63. Thermometry is performed on resonance at $f_0 = 593$ MHz, where the phase is most responsive.

of the device and to create a good rf ground at the frequency of operation. A 96-kΩ resistor is used to prevent rf signals from escaping via the dc-bias line. The resonant frequency depends on the total top-gate capacitance via $f_0 = 1/2\pi\sqrt{L(C_c + C_p + C_t)}$. At the circuit resonant frequency, $\phi \propto C_t$, when $C_t \ll C_p + C_c$ [17,28,30–32]. This gives a change in reflected-signal phase that depends on T_e according to

$$\phi - \phi_0 = Ae\alpha\left(f' * n\right), \tag{7}$$

where A is a fitting constant, which tells us the phase change due to a small change in capacitance, and ϕ_0 is the circuit phase offset at the resonant frequency when $C_t \approx 0$. If the constants A, α, and Γ are known, measurement of $\phi - \phi_0$ as a function of $V_{tg} - V_0$ and fitting of the model described by Eq. (7) gives a readout of the electron temperature T_e. A demonstration of this technique is shown in Fig. 3.

III. RESULTS

The QD thermometer is installed in two fridge systems: a cryogen-free 1 K cryostat [33] and a cryogen-free dilution refrigerator [34], where it is calibrated and operated. In both systems, the fridge temperature is monitored by a ruthenium oxide resistance fridge thermometer [35], mounted alongside the QD thermometer during data collection. The reading of the ruthenium oxide fridge thermometer is denoted as T_f.

In the 1-K cryostat, calibration is done by reading the reflected-signal phase across a number of sweeps of V_{tg} at a set of fridge temperatures $T_f = 2.0$, 2.5, and 3.0 K. A single least-squares fit using Eq. (7) is performed on the collective phase traces for this set of temperatures (Fig. 3). It is assumed that the electron temperature is well thermalized with the fridge temperature at 2 K and above and so during the calibration the condition $T_e = T_f$ is applied to Eq. (7). For each phase trace, ϕ_0 and V_0 are individually fitted. The calibration fit produces an estimate for the values $\alpha = 0.74 \pm 0.02$, $\Gamma = 270 \pm 20\ \mathrm{ns}^{-1}$, and $A = 5.13 \pm 0.06\ \mathrm{rad\,pF}^{-1}$. This implies that $\Gamma \gg 2\pi f_0$; therefore, dissipative components are neglected and the cyclic tunneling is considered adiabatic. With these three constants defined, the thermometer is calibrated and ready for operation.

To use the QD thermometer, $\phi - \phi_0$ is measured as a function of $V_{tg} - V_0$ and fitted with the calibrated Eq. (7) to give a readout of the electron temperature T_e. A series of

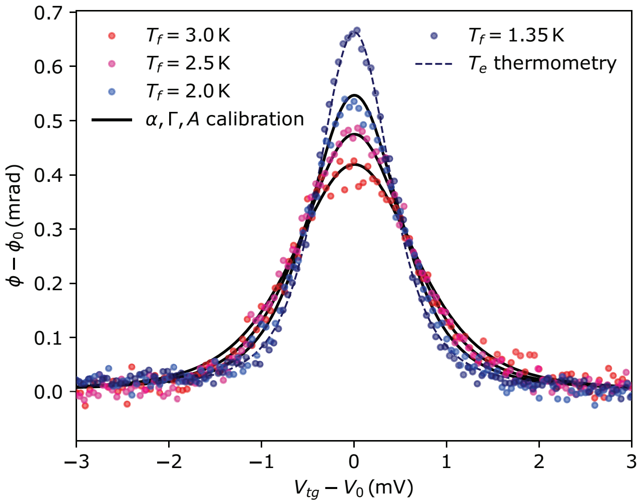

FIG. 3. The QD-thermometer calibration in 1 K cryostat, showing three experimental phase traces taken at fridge temperatures $T_f = 2.0$, 2.5, and 3.0 K. Each trace shows the change in reflected-signal phase $\phi - \phi_0$ against the top-gate voltage $V_{tg} - V_0$ around the Coulomb peak of the QD. The solid black lines show the least-squares fit of Eq. (7) onto the data, assuming that the electron temperature T_e equals the fridge thermometer readout T_f. This calibration procedure estimates $\alpha = 0.74 \pm 0.02$, $\Gamma = 270 \pm 20$ ns^{-1}, and $A = 5.13 \pm 0.06$ rad pF^{-1}. These three constants are then included within Eq. (7), allowing electron thermometry to be performed, shown here with a T_e fit to data taken at $T_f = 1.35$ K, yielding an electron temperature $T_e = 1.4 \pm 0.1$ K.

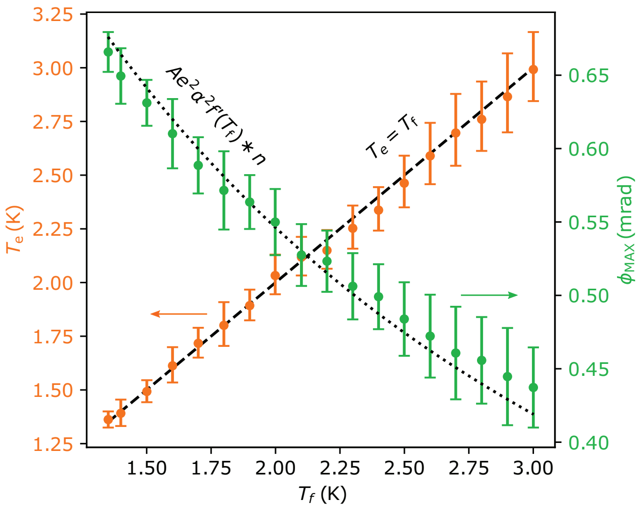

FIG. 4. The electron temperature T_e (orange) and the maximum phase $\phi_{\rm MAX}$ (green) readout from the QD thermometer in the 1-K cryostat. The thermometry readout is generated by fitting T_e, via the calibrated Eq. (7), to the phase curve observed by sweeping the V_{tg} over the QD Coulomb peak. The peak phase $\phi_{\rm MAX}$ is measured at $V_{tg} = V_0$, with no fitting process required. The fridge temperature T_f is read from a ruthenium oxide fridge thermometer thermally linked to the QD device. The dashed line highlights where $T_e = T_f$. The dotted line represents the model prediction from the calibrated Eq. (7), assuming $T_e = T_f$.

thermometry readings are taken at varying fridge temperatures between 3.0 K and 1.3 K. The fridge temperature T_f is monitored for each QD thermometer reading of T_e (Fig. 4). The QD thermometer agrees with the fridge thermometer across the range of temperatures, even at temperatures below the calibration range. It is worth noting that this works in the intermediate regime where $k_B T \sim \hbar\Gamma$ because the tunnel broadening is taken into account within the physical model. For a quicker electron-temperature readout, the QD can be tuned to where $V_{tg} = V_0$, so that $\phi - \phi_0 = \phi_{\rm MAX}$, which is directly converted to a electron temperature via Eq. (7), using the previously calibrated values of α, Γ, and A. This approach works effectively even at fridge temperatures below the calibration data.

Finally, to provide an independent confirmation of the calibration process, the QD source and drain connections are ungrounded to apply a source-drain voltage V_{SD} across the QD and measure a charge-stability diagram of the device. Using the relationship

$$\alpha = \frac{1}{m_d - m_s}, \tag{8}$$

where $m_d = \Delta V^d_{tg}/\Delta V^d_{SD}$ is the gradient along the "drain resonance" side of a Coulomb diamond and $m_s = \Delta V^s_{tg}/\Delta V^s_{SD}$ is the "source-resonance" side, we can see that the lever arm $\alpha = 0.74 \pm 0.02$ matches well with the Coulomb diamond geometry in Fig. 5. This demonstrates that the lever arm of a QD can be obtained using one nongalvanic gate connection and measurements spanning a range of fridge temperatures. The order of magnitude of the source-drain current $|I_{SD}|$ from the unblockaded QD is found to be in the order of approximately 10 nA. This agrees with the calibration fit of the total tunnel-rate constant 270 ± 20 ns^{-1}, which equates to a source-drain current of $e\Gamma = 6.9 \pm 0.5$ nA for a single-electron transport channel.

To study operation at lower temperatures, the QD thermometer is mounted into a dilution refrigerator. The calibration fit is performed as described above, with phase data taken at 1300 mK and 1600 mK. Within this system, the three calibration constants are found to be $\alpha = 0.84 \pm 0.03$, $\Gamma = 510 \pm 10$ ns^{-1}, and $A = 0.75 \pm 0.07$ rad pF^{-1}. The change in A is attributed to the differences between the two fridge systems affecting the rf electronics, such as the parasitic capacitance C_p changing due to a different metallic geometry near the QD chip. Both α and Γ are sensitive to the shape and position of the QD in the Si channel, which are likely to be different after a thermal cycle of the device.

The electron-temperature readout T_e from the QD thermometer in the dilution refrigerator agrees with the fridge

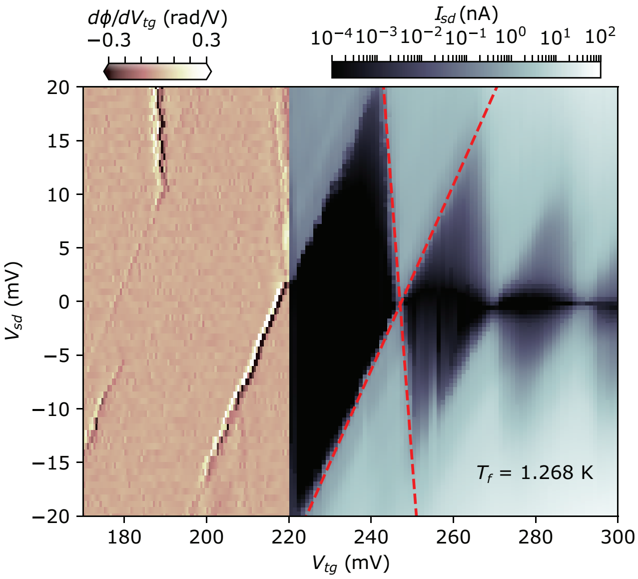

FIG. 5. The charge-stability diagram measured by reflectometry technique and dc transport in the 1-K cryostat. To the left of $V_{tg} = 220$ mV, the derivative of the reflected-signal phase with respect to the top-gate voltage $d\phi/\mathrm{d}V_{tg}$ is plotted, demonstrating the nongalvanic reflectometry technique. For this measurement, the source and drain connections are grounded. To the right of $V_{tg} = 220$ mV, the QD source-drain current $|I_{SD}|$ is plotted on a log scale. The fridge temperature is $T_f = 1.268 \pm 0.001$ K. The red lines highlight the source-drain gradients that match the calibration fit lever-arm prediction, $\alpha = 0.74 \pm 0.02$, via Eq. (8), crossing at the QD Coulomb peak where the thermometry takes place. Here, the on-resonance current has an order of magnitude $I_{SD} \approx 1 - 10$ nA, which is similar to that of the single-electron current defined by the calibration fit tunnel rate $e\Gamma \sim 6.9 \pm 0.5$ nA.

temperature readout T_f above 1 K, despite the fact that $k_B T_f < \hbar\Gamma$ [Fig. 6(a)]. Below 1 K there is a deviation of T_e away from T_f, although the point $T_e = T_f$ remains within one standard deviation of the experimental uncertainty (for details on how the error is determined, see Sec. II in the Supplemental Material [36]). The deviation of the T_e readout and its increase in uncertainty occur because the QD energy level is strongly tunnel broadened and the response of the phase trace to the temperature becomes weaker (for details on the influence of tunnel broadening, see Sec. III in the Supplemental Material [36]). With a reduced Γ, the QD thermometer would work at lower temperatures. This can be achieved by adjusting the device design geometry. Checking the charge-stability diagram, the predicted lever arm $\alpha = 0.84 \pm 0.03$ matches the Coulomb diamond geometry well [Fig. 6(b)]. The dilution refrigerator experiment has an average white-noise phase sensitivity of 1.1 ± 0.1 $\mu\mathrm{rad}/\sqrt{\mathrm{Hz}}$, in this case dominated by the measurement chain. With this equipment and the ϕ_{MAX} measurements demonstrated in Fig. 4, the QD thermometer setup could achieve a potential sensitivity of 11 ± 1 $\mathrm{mK}/\sqrt{\mathrm{Hz}}$ at 3.0 K, and 4.0 ± 0.3 $\mathrm{mK}/\sqrt{\mathrm{Hz}}$ at 1.3 K (for details on the thermometer sensitivity, see Sec. I in the Supplemental Material [36]).

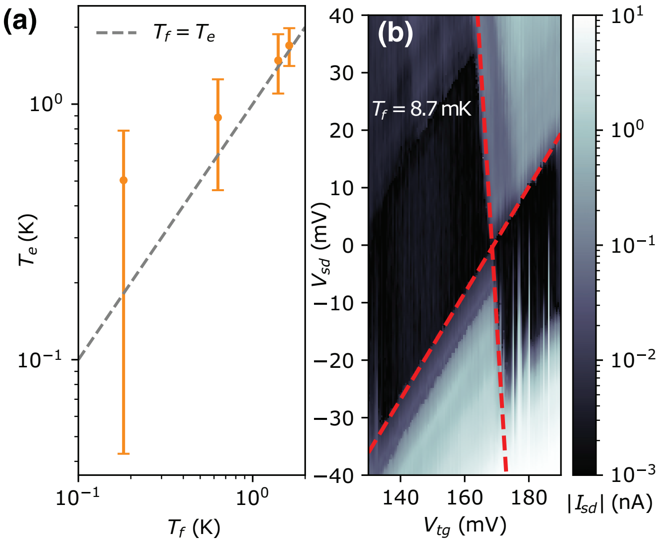

FIG. 6. QD The thermometry and stability diagram from the dilution-refrigerator measurements. (a) The recalibrated QD thermometer readout of the electron temperature T_e compared with the fridge-thermometer readout T_f, measured near the device within the dilution refrigerator. The QD and fridge thermometers start to disagree below 1 K but still agree to within one standard deviation of confidence [37] (for details on how the error is determined, see Sec. II in the Supplemental Material [36]). (b) The source-drain current-stability diagram of the QD mounted in the dilution refrigerator. The temperature of the fridge is held at $T_f = 8.70 \pm 0.05$ mK. The red lines highlight the source-drain gradients that match the calibration fit lever-arm prediction, $\alpha = 0.84 \pm 0.03$, via Eq. (8), crossing at the QD Coulomb peak where the thermometry takes place.

IV. CONCLUSIONS

We describe the successful calibration and operation of a QD-thermometer readout via a single capacitive connection in two separate cryostats, which provides a simple and versatile way to measure the electron temperature. The calibration uses limited data to generate a physical model of the QD-reservoir system, which correctly estimates physical parameters such as the QD lever arm. The electron thermometry is successfully performed with the calibrated QD thermometer in a temperature range of 1.0–3.0 K. The QD thermometer is also used for faster readout by monitoring the phase when the QD has an occupation probability of 1/2. In this mode of operation, the noise floor of the measurement should allow for a sensitivity of 4.0 ± 0.3 $\mathrm{mK}/\sqrt{\mathrm{Hz}}$ and 11 ± 1 $\mathrm{mK}/\sqrt{\mathrm{Hz}}$, at 1.3 K and 3.0 K, respectively. This process works with the same QD chip in both cryostats. The QD thermometer can operate even in the case in which $k_B T_e < \hbar\Gamma$; however, with the system and techniques used here, the thermometry uncertainty starts to increase below 1 K, due to strong tunnel coupling overriding the temperature dependence. Careful analysis of the thermometry uncertainty reveals the coldest limit of the QD thermometer, when the electron-temperature readout confidence boundary increases beyond a usable size. A redesign of the QD device to reduce the tunnel rate would be needed to decrease the uncertainty at lower temperatures. The ability to fully calibrate and operate a nongalvanic electron thermometer with a single rf line simplifies the application of the device substantially. This device provides a versatile, sensitive, and effective tool for monitoring the electron temperature in nanoelectronic devices at cryogenic temperatures.

The data that support the findings of this study are available online [38], including descriptions of the data sets.

ACKNOWLEDGMENTS

We thank Xiao Collins, Kunal Lulla Ramrakhiyani, Michael Thompson, and Alex Jones for their assistance. This work was funded and supported by the European Microkelvin Platform (the European Union's Horizon 2020 research and innovation program, under Grant Agreement No. 824109), the United Kingdom Engineering and Physical Sciences Research Council (EPSRC) (Grant No. EP/N019199/1), the European Research Council (ERC) (Grant No. 818751), and Hitachi Europe Ltd.

[1] F. Giazotto, T. T. Heikkilä, A. Luukanen, A. M. Savin, and J. P. Pekola, Opportunities for mesoscopics in thermometry and refrigeration: Physics and applications, Rev. Mod. Phys. **78**, 217 (2006).

[2] C. Beenakker, Theory of Coulomb-blockade oscillations in the conductance of a quantum dot, Phys. Rev. B **44**, 1646 (1991).

[3] J. Pekola, K. Hirvi, J. Kauppinen, and M. Paalanen, Thermometry by Arrays of Tunnel Junctions, Phys. Rev. Lett. **73**, 2903 (1994).

[4] L. Spietz, K. Lehnert, I. Siddiqi, and R. Schoelkopf, Primary electronic thermometry using the shot noise of a tunnel junction, Science **300**, 1929 (2003).

[5] D. Maradan, L. Casparis, T.-M. Liu, D. Biesinger, C. Scheller, D. Zumbühl, J. Zimmerman, and A. Gossard, GaAs quantum dot thermometry using direct transport and charge sensing, J. Low Temp. Phys. **175**, 784 (2014).

[6] J. V. Koski, A. Kutvonen, I. M. Khaymovich, T. Ala-Nissila, and J. P. Pekola, On-Chip Maxwell's Demon as an Information-Powered Refrigerator, Phys. Rev. Lett. **115**, 260602 (2015).

[7] D. I. Bradley, R. E. George, D. Gunnarsson, R. P. Haley, H. Heikkinen, Y. A. Pashkin, J. Penttilä, J. R. Prance, M. Prunnila, L. Roschier, *et al.*, Nanoelectronic primary thermometry below 4 mK, Nat. Commun. **7**, 1 (2016).

[8] O. Hahtela, E. Mykkänen, A. Kemppinen, M. Meschke, M. Prunnila, D. Gunnarsson, L. Roschier, J. Penttilä, and J. Pekola, Traceable Coulomb blockade thermometry, Metrologia **54**, 69 (2016).

[9] Z. Iftikhar, A. Anthore, S. Jezouin, F. Parmentier, Y. Jin, A. Cavanna, A. Ouerghi, U. Gennser, and F. Pierre, Primary thermometry triad at 6 mK in mesoscopic circuits, Nat. Commun. **7**, 1 (2016).

[10] G. Nicolí, P. Märki, B. A. Bräm, M. P. Röösli, S. Hennel, A. Hofmann, C. Reichl, W. Wegscheider, T. Ihn, and K. Ensslin, Quantum dot thermometry at ultra-low temperature in a dilution refrigerator with a ^{4}He immersion cell, Rev. Sci. Instrum. **90**, 113901 (2019).

[11] A. Jones, C. Scheller, J. Prance, Y. Kalyoncu, D. Zumbühl, and R. Haley, Progress in cooling nanoelectronic devices to ultra-low temperatures, J. Low Temp. Phys. **201**, 772 (2020).

[12] L. DiCarlo, H. Lynch, A. Johnson, L. Childress, K. Crockett, C. Marcus, M. Hanson, and A. Gossard, Differential Charge Sensing and Charge Delocalization in a Tunable Double Quantum Dot, Phys. Rev. Lett. **92**, 226801 (2004).

[13] P. Torresani, M. Martínez-Pérez, S. Gasparinetti, J. Renard, G. Biasiol, L. Sorba, F. Giazotto, and S. De Franceschi, Nongalvanic primary thermometry of a two-dimensional electron gas, Phys. Rev. B **88**, 245304 (2013).

[14] A. Mavalankar, S. Chorley, J. Griffiths, G. Jones, I. Farrer, D. Ritchie, and C. Smith, A non-invasive electron thermometer based on charge sensing of a quantum dot, Appl. Phys. Lett. **103**, 133116 (2013).

[15] J. Prance, C. Smith, J. Griffiths, S. Chorley, D. Anderson, G. Jones, I. Farrer, and D. Ritchie, Electronic Refrigeration of a Two-Dimensional Electron Gas, Phys. Rev. Lett. **102**, 146602 (2009).

[16] S. Gasparinetti, K. Viisanen, O.-P. Saira, T. Faivre, M. Arzeo, M. Meschke, and J. Pekola, Fast Electron Thermometry for Ultrasensitive Calorimetric Detection, Phys. Rev. Appl. **3**, 014007 (2015).

[17] I. Ahmed, A. Chatterjee, S. Barraud, J. J. Morton, J. A. Haigh, and M. F. Gonzalez-Zalba, Primary thermometry of a single reservoir using cyclic electron tunneling to a quantum dot, Commun. Phys. **1**, 1 (2018).

[18] A. Betz, S. Barraud, Q. Wilmart, B. Placais, X. Jehl, M. Sanquer, and M. Gonzalez-Zalba, High-frequency characterization of thermionic charge transport in silicon-on-insulator nanowire transistors, Appl. Phys. Lett. **104**, 043106 (2014).

[19] B. Voisin, V.-H. Nguyen, J. Renard, X. Jehl, S. Barraud, F. Triozon, M. Vinet, I. Duchemin, Y.-M. Niquet, S. De Franceschi, *et al.*, Few-electron edge-state quantum dots in a silicon nanowire field-effect transistor, Nano Lett. **14**, 2094 (2014).

[20] D. J. Ibberson, L. Bourdet, J. C. Abadillo-Uriel, I. Ahmed, S. Barraud, M. J. Calderón, Y.-M. Niquet, and M. F. Gonzalez-Zalba, Electric-field tuning of the valley splitting in silicon corner dots, Appl. Phys. Lett. **113**, 053104 (2018).

[21] L. P. Kouwenhoven, C. M. Marcus, P. L. McEuen, S. Tarucha, R. M. Westervelt, and N. S. Wingreen, in *Mesoscopic Electron Transport* (Springer, Dordrecht, 1997), p. 105.

[22] T. Ihn, *Semiconductor Nanostructures: Quantum States and Electronic Transport* (Oxford University Press, Oxford, 2010).

[23] N. Hartman, C. Olsen, S. Lüscher, M. Samani, S. Fallahi, G. C. Gardner, M. Manfra, and J. Folk, Direct entropy measurement in a mesoscopic quantum system, Nat. Phys. **14**, 1083 (2018).

[24] M. Esterli, R. Otxoa, and M. Gonzalez-Zalba, Small-signal equivalent circuit for double quantum dots at low-frequencies, Appl. Phys. Lett. **114**, 253505 (2019).

[25] R. Mizuta, R. Otxoa, A. Betz, and M. F. Gonzalez-Zalba, Quantum and tunneling capacitance in charge and spin qubits, Phys. Rev. B **95**, 045414 (2017).

[26] S. Shevchenko, A. Omelyanchouk, and E. Il'ichev, Multiphoton transitions in Josephson-junction qubits, J. Low Temp. Phys. **38**, 283 (2012).

[27] S. Shevchenko, S. Ashhab, and F. Nori, Inverse Landau-Zener-Stückelberg problem for qubit-resonator systems, Phys. Rev. B **85**, 094502 (2012).

[28] G. Johansson, L. Tornberg, V. Shumeiko, and G. Wendin, Readout methods and devices for Josephson-junction-based solid-state qubits, J. Phys. Condens. Matter **18**, S901 (2006).

[29] I. Ahmed, J. A. Haigh, S. Schaal, S. Barraud, Y. Zhu, C.-m. Lee, M. Amado, J. W. Robinson, A. Rossi, J. J. Morton, *et al.*, Radio-Frequency Capacitive Gate-Based Sensing, Phys. Rev. Appl. **10**, 014018 (2018).

[30] S. Chorley, J. Wabnig, Z. Penfold-Fitch, K. Petersson, J. Frake, C. Smith, and M. Buitelaar, Measuring the Complex Admittance of a Carbon Nanotube Double Quantum Dot, Phys. Rev. Lett. **108**, 036802 (2012).

[31] A. Betz, R. Wacquez, M. Vinet, X. Jehl, A. Saraiva, M. Sanquer, A. Ferguson, and M. Gonzalez-Zalba, Dispersively detected Pauli spin-blockade in a silicon nanowire field-effect transistor, Nano Lett. **15**, 4622 (2015).

[32] M. F. Gonzalez-Zalba, S. N. Shevchenko, S. Barraud, J. R. Johansson, A. J. Ferguson, F. Nori, and A. C. Betz, Gate-sensing coherent charge oscillations in a silicon field-effect transistor, Nano Lett. **16**, 1614 (2016).

[33] Oxford Instruments "Io".

[34] BlueFors "LD250".

[35] Model reference "ROTH-GEN" in the 1-K cryostat and "RuO2.RX-102B" in the dilution refrigerator.

[36] See the Supplemental Material at http://link.aps.org/supplemental/10.1103/PhysRevApplied.15.034044 for extra material on the quantum dot thermometer temperature sensitivity, the electron-thermometry error, the quantum dot energy scales, and the Coulomb-peak-location temperature dependence.

[37] W. H. Press, S. A. Teukolsky, W. T. Vetterling, and B. P. Flannery, *Numerical Recipes 3rd Edition: The Art of Scientific Computing* (Cambridge University Press, New York, 2007).

[38] J. M. A. Chawner, S. Barraud, M. F. Gonzalez-Zalba, S. Holt, E. A. Laird, Yu. A. Pashkin, and J. R. Prance, Data for: "Nongalvanic calibration and operation of a quantum dot thermometer," https://doi.org/10.17635/lancaster/researchdata/403 (2021).